ARTICLE

Cation vacancy stabilization of single-atomic-site Pt$_1$/Ni(OH)$_x$ catalyst for diboration of alkynes and alkenes

Jian Zhang [1], Xi Wu[2], Weng-Chon Cheong [1], Wenxing Chen [1], Rui Lin[1], Jia Li [2], Lirong Zheng[3], Wensheng Yan[4], Lin Gu[5], Chen Chen[1], Qing Peng[1], Dingsheng Wang [1] & Yadong Li[1]

Development of single-atomic-site catalysts with high metal loading is highly desirable but proved to be very challenging. Although utilizing defects on supports to stabilize independent metal atoms has become a powerful method to fabricate single-atomic-site catalysts, little attention has been devoted to cation vacancy defects. Here we report a nickel hydroxide nanoboard with abundant Ni^{2+} vacancy defects serving as the practical support to achieve a single-atomic-site Pt catalyst (Pt$_1$/Ni(OH)$_x$) containing Pt up to 2.3 wt% just by a simple wet impregnation method. The Ni^{2+} vacancies are found to have strong stabilizing effect of single-atomic Pt species, which is determined by X-ray absorption spectrometry analyses and density functional theory calculations. This Pt$_1$/Ni(OH)$_x$ catalyst shows a high catalytic efficiency in diboration of a variety of alkynes and alkenes, yielding an overall turnover frequency value upon reaction completion for phenylacetylene of ~3000 h^{-1}, which is much higher than other reported heterogeneous catalysts.

[1] Department of Chemistry, Tsinghua University, 100084 Beijing, China. [2] Laboratory for Computational Materials Engineering, Division of Energy and Environment, Graduate School at Shenzhen, Tsinghua University, 518055 Shenzhen, China. [3] Beijing Synchrotron Radiation Facility, Institute of High Energy Physics, Chinese Academy of Sciences, 100049 Beijing, China. [4] National Synchrotron Radiation Laboratory, CAS Center for Excellence in Nanoscience, University of Science and Technology of China, 230029 Hefei, China. [5] Beijing National Laboratory for Condensed Matter Physics, Institute of Physics, Chinese Academy of Sciences, 100190 Beijing, China. These authors contributed equally: Jian Zhang, Xi Wu. Correspondence and requests for materials should be addressed to D.W. (email: wangdingsheng@mail.tsinghua.edu.cn) or to Y.L. (email: ydli@mail.tsinghua.edu.cn)

Single-atomic-site (SAS) heterogeneous catalysts have attracted much recent interest owing to their specific activity and maximum atom efficiency for low cost[1–10]. However, synthesis of such SAS catalysts is not trivial because isolated metal atoms are often very mobile and easy to sinter under realistic reaction conditions due to their high surface free energy[2,4]. For this reason, most available SAS catalysts must keep a low loading density of guest metals (usually <0.5 weight percent (wt%)) to resist their aggregation, and it remains a great challenge to improve the loading content in such catalysts for practical applications[5]. Exploiting defects on supports to enhance the interaction between individual metal atoms and the supports has been an effective strategy to fabricate SAS catalysts[11–22]. So far, much work has focused on oxygen vacancy defects on oxides and carbon vacancy defects on graphene[11–18]. Cation vacancies are another kind of classical defects but are comparatively little investigated in the research field of SAS catalysts[19–22], probably because of their difficult characterization and scarce suitable support materials with such defects[23]. Hydroxides are a large class of functional, environmentally friendly, and inexpensive host materials[24]. As far as we know, the cation vacancies on hydroxides have never been reported, and utilizing the defect-rich hydroxide to achieve a high metal-loading SAS catalyst has not been realized yet.

Boronic acids and their derivatives are versatile and useful compounds for various applications in organic synthesis[25], material science[26], and biomedicine[27]. Over the past decades, a broad variety of transition-metal-catalyzed protocols have been developed for the preparation of these compounds[28]. Among them, the diboration of carbon–carbon multiple bonds represents a straightforward and atom-economic strategy[29]. Since the first discovery of the Pt-catalyzed diboration of alkynes by Suzuki and Miyaura et al. in 1993, various homogeneous transition-metal catalysts have been successfully applied into the diboration of alkynes or alkenes[29–35]. However, up to now, the development of heterogeneous catalysts for such diboration reactions lags far behind the homogeneous catalysts with limited reported cases that include Pd/C[36], nanoporous-gold[37], Pt/TiO$_2$[38], and Pt/MgO[39]. To make matter worse, these heterogeneous catalysts are restricted in practical application for their low catalytic efficiency (overall turnover frequency (TOF$_{overall}$) upon reaction completion <50 h^{-1}). There is thereby an urgent need to prepare a new heterogeneous catalyst with better catalytic efficiency for diboration reactions. Given that the catalytically active components in these reported catalysts are all metal nanoparticles and downsizing metal particles to single atoms is ordinarily a great impetus to improve the performance of a catalyst[4,5], we expect that the rational design of SAS catalysts will offer exciting opportunities to achieve the ideal heterogeneous catalysts for diboration reactions.

Here we report that a defect-rich nickel hydroxide (Ni(OH)$_x$) nanoboards (NBs) supported SAS Pt catalyst (Pt$_1$/Ni(OH)$_x$) fabricated by a simple wet impregnation method. Notably, although there have been a few reports on the combination of nickel hydroxides with Pt nanoparticles, the construction of SAS Pt species on nickel hydroxides has never been achieved[40–42]. In this work, a new polycrystalline Ni(OH)$_x$ NBs are synthesized on a large scale via a one-pot solvothermal procedure. The abundant Ni^{2+} vacancy defects on the Ni(OH)$_x$ NBs are shown to be critical for preparing Pt$_1$/Ni(OH)$_x$ with Pt loading up to 2.3 wt%. The as-prepared Pt$_1$/Ni(OH)$_x$ catalyst exhibits a good performance for the diboration of alkynes and alkenes. A TOF$_{overall}$ upon reaction completion much greater than that of all reported heterogeneous catalysts is demonstrated on Pt$_1$/Ni(OH)$_x$ in the diboration of alkynes.

Results

Synthesis and characterization of the Pt$_1$/Ni(OH)$_x$ catalyst. To prepare the Pt$_1$/Ni(OH)$_x$ catalyst, a polycrystalline Ni(OH)$_x$ NB material was first synthesized on a large scale through a solvothermal reaction between nickel nitrate (Ni(NO$_3$)$_2$·6H$_2$O), urea, sodium bicarbonate (NaHCO$_3$), and tetrabutylammonium hydroxide (TBAH) in water/triethylene glycol mixed solvent (for details, see the Methods section). The typical transmission electron microscopic (TEM) image clearly illustrates that the as-synthesized samples display a uniformly NB morphology (Fig. 1a). Clear irregular crystal lattice fringes are observed on the NBs in the high-resolution TEM (HR-TEM) image (Fig. 1b), indicating the polycrystalline structure of the sample, which is further proved by the selected-area electron diffraction pattern and X-ray diffraction (XRD) pattern (Supplementary Figs. 1 and 2). X-ray photoelectron spectroscopy (XPS) and Fourier transform infrared spectroscopy (FT-IR) of this polycrystalline NBs both exhibit features that are typical nickel hydroxide (Supplementary Fig. 3). To the best of our knowledge, this one-dimensional polycrystalline nanostructures of nickel hydroxide are newly synthesized by our work, which are more challenging in synthesis compared with common nickel hydroxide nanosheets[43,44].

The Pt$_1$/Ni(OH)$_x$ catalyst was then prepared with the as-synthesized Ni(OH)$_x$ NB material as a support by a wet impregnation method, which stands for an easy-handling, straightforward, and low-cost pathway to synthesize catalysts[45,46]. Hexachloroplatinic acid (H$_2$PtCl$_6$) was introduced into an ethanol dispersion of Ni(OH)$_x$ NBs to allow the adsorption of Pt precursors. The mixture was then centrifuged and the recovered solid was reduced with hydrogen to provide the Pt$_1$/Ni(OH)$_x$ catalyst (for details, see the Methods section). Scanning transmission electron microscopy (STEM) images and XRD detections of the obtained Pt$_1$/Ni(OH)$_x$ reveal that no formation of Pt nanoparticles are observed on Ni(OH)$_x$ NBs, even with the
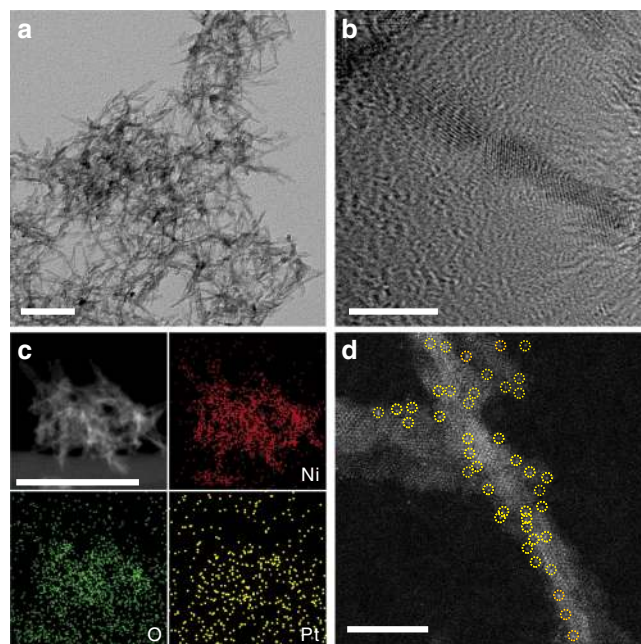

Fig. 1 Characterization of Ni(OH)$_x$ NBs and the Pt$_1$/Ni(OH)$_x$ catalyst. **a** TEM image of Ni(OH)$_x$ NBs. Scale bar, 50 nm. **b** HR-TEM image of a Ni(OH)$_x$ nanoboard. Scale bar, 20 nm. **c** EDX elemental mapping analysis of the Pt$_1$/Ni(OH)$_x$ catalyst. Scale bar, 100 nm. **d** Representative AC HAADF-STEM image of the Pt$_1$/Ni(OH)$_x$ catalyst. The yellow circles were drawn around SAS Pt. Scale bar, 10 nm

loading amount of Pt as high as 2.3 wt% as analyzed by inductively coupled plasma optical emission spectrometry (ICP-OES) (Supplementary Fig. 4). Further energy-dispersive X-ray (EDX) elemental mapping analysis confirms that Pt species are evenly dispersed in $Pt_1/Ni(OH)_x$ (Fig. 1c). To verify the SAS Pt species on the $Ni(OH)_x$ NBs, we performed the aberration-corrected high-angle annular dark-field STEM (AC HAADF-STEM) measurements on $Pt_1/Ni(OH)_x$ (Fig. 1d). It is clear that all the Pt species exist exclusively at isolated single atomic sites; neither subnanometer clusters nor nanoparticles are detected.

The presence of SAS Pt can be further confirmed by X-ray absorption spectrometric (XAS) studies. Figure 2a represents the extended X-ray absorption fine structure (EXAFS) spectrum of $Pt_1/Ni(OH)_x$ and the reference spectra of Pt foil and PtO_2 at the Pt L_3-edge using a Fourier transform (for corresponding EXAFS in K-space, see Supplementary Fig. 5). There is one prominent peak at ~1.6 Å from the Pt–O contribution and a relatively weak peak at ~2.9 Å from the Pt–Ni contribution but no peak at ~2.6 Å from the Pt–Pt contribution, confirming the sole presence of SAS Pt in the $Pt_1/Ni(OH)_x$ catalyst. Moreover, the oxidation state of these SAS Pt is determined by the X-ray absorption near-edge structure (XANES) spectra, as shown in Fig. 2b. The white-line intensities in the spectra reflect the oxidation state of Pt in different samples, so the white-line intensity of $Pt_1/Ni(OH)_x$, which is close to that of PtO_2, implies that the SAS Pt in the $Pt_1/Ni(OH)_x$ catalyst still remain in a high oxidation state even after the reduction by hydrogen.

Catalytic performance evaluation for diboration reactions. We next investigated the catalytic activity of the as-prepared $Pt_1/Ni(OH)_x$ for diboration reactions. Initially, the diboration of phenylacetylene (1a) with bis(pinacolato)diboron (B_2pin_2) (2a) was chosen as a model reaction (Supplementary Table 1, entry 1). To our delight, the $Pt_1/Ni(OH)_x$ displayed a high activity and selectivity for this reaction. The conversion of phenylacetylene attained 97% within 20 min at a molar ration of $1:10^3$ (Pt: phenylacetylene), and bare of other by-products like hydroborylated product were observed by gas chromatography–mass spectrometer (GC-MS) analysis (Supplementary Fig. 6). The calculated $TOF_{overall}$ value of $Pt_1/Ni(OH)_x$ upon this reaction completion can reach a high level as ~3000 h^{-1}, much higher than that of other heterogeneous catalysts reported previously. In contrast, no reaction occurred when using $Ni(OH)_x$ NBs as the catalyst without Pt (Supplementary Table 1, entry 2). The catalyst can be reused at least five times without any loss of selectivity although the activity has a slight decay (Supplementary Fig. 7). STEM and AC HAADF-STEM characterizations reveal that no morphology changes and Pt components are still dispersed at isolated single

atomic sites in the recovered catalyst (Supplementary Fig. 8). Moreover, the expansion of the reaction scale has no effect on the catalytic efficiency of this $Pt_1/Ni(OH)_x$ catalyst for such diboration reactions (Supplementary Fig. 9). We further investigated the substrate scope of the diboration reactions to study the influence of substrate categories on the catalytic efficiency of $Pt_1/Ni(OH)_x$. As shown in Fig. 3, the aryl alkynes bearing electron-donating groups (R = Me, OMe) can react smoothly with B_2pin_2 over $Pt_1/Ni(OH)_x$ at the same conversion rate of phenylacetylene, affording the corresponding products **3ba** and **3ca** in excellent yields. When the substituents are electron-withdrawing groups (R = Cl, Br, NO_2) on the aryl ring, however, a longer reaction time is required to give the target molecular **3da–3fa** in high yields. Differently from substituent types, substituent positions have no influence on the catalytic efficiency of $Pt_1/Ni(OH)_x$, whether *meta*-methyl or *ortho*-methyl substituted phenylacetylene can completely transform into the products **3ga** and **3ha** without any loss in the reaction rate. As for diboration of internal aryl alkynes like diphenylacetylene, $Pt_1/Ni(OH)_x$ suffers from a relatively low catalytic activity, although a complete conversion of the substrate and a quantitative selectivity of diborylated product **3ia** can be also achieved. To our delight, different kinds of aliphatic alkynes are appropriate for the diboration reactions over $Pt_1/Ni(OH)_x$ as well, furnishing the desired products **3ja–3la** with the similar reaction efficiency to the terminal aryl alkynes. Besides the various alkynes, different boronate esters like bis(neo-pentylglycolate)diboron (B_2neop_2) can also work well with phenylacetylene to provide the product **3ab** in an excellent yield and selectivity at the same reaction rate of B_2pin_2. Even more, alkenes were also chosen as substrates to evaluate the catalytic performance of $Pt_1/Ni(OH)_x$ for diboration reactions. It shows that the diboration of styrene and 1-octene catalyzed by $Pt_1/Ni(OH)_x$ can proceed well and provide a selectivity to products **3ma** and **3na** of 99% at the conversion level of 90% and 86%, respectively, although the reaction rates are lower than that of alkynes with similar molecular structures.

Discussion

Apparently, the good catalytic performance of $Pt_1/Ni(OH)_x$ derives from the high loading content of Pt at isolated single atomic sites. It is noteworthy that such a high loading density of SAS catalyst is quite difficult in fabrication through the wet impregnation method[47–50]. The impregnated metal precursors generally adsorb on the surface of supports and thus tend to aggregate to form clusters or nanoparticles easily during the post-treatment processes[1]. For comparison, a conventional perfect Ni$(OH)_2$ material was synthesized and impregnated with H_2PtCl_6 with a lower Pt loading at 0.9 wt% (as determined by ICP-OES)

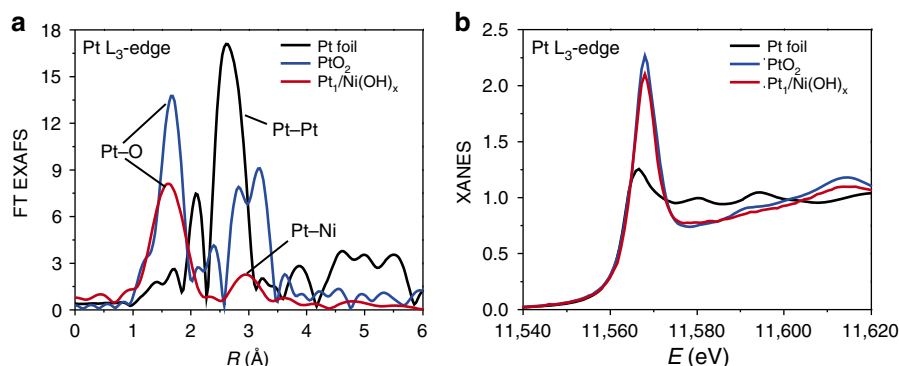**Fig. 2** X-ray absorption spectrometric studies of the $Pt_1/Ni(OH)_x$ catalyst. **a** Fourier transform EXAFS spectrum of the $Pt_1/Ni(OH)_x$ catalyst in comparison with PtO_2 and Pt foil at the Pt L_3-edge. **b** XANES spectra at the Pt L_3-edge of the $Pt_1/Ni(OH)_x$ catalyst, PtO_2, and Pt foil
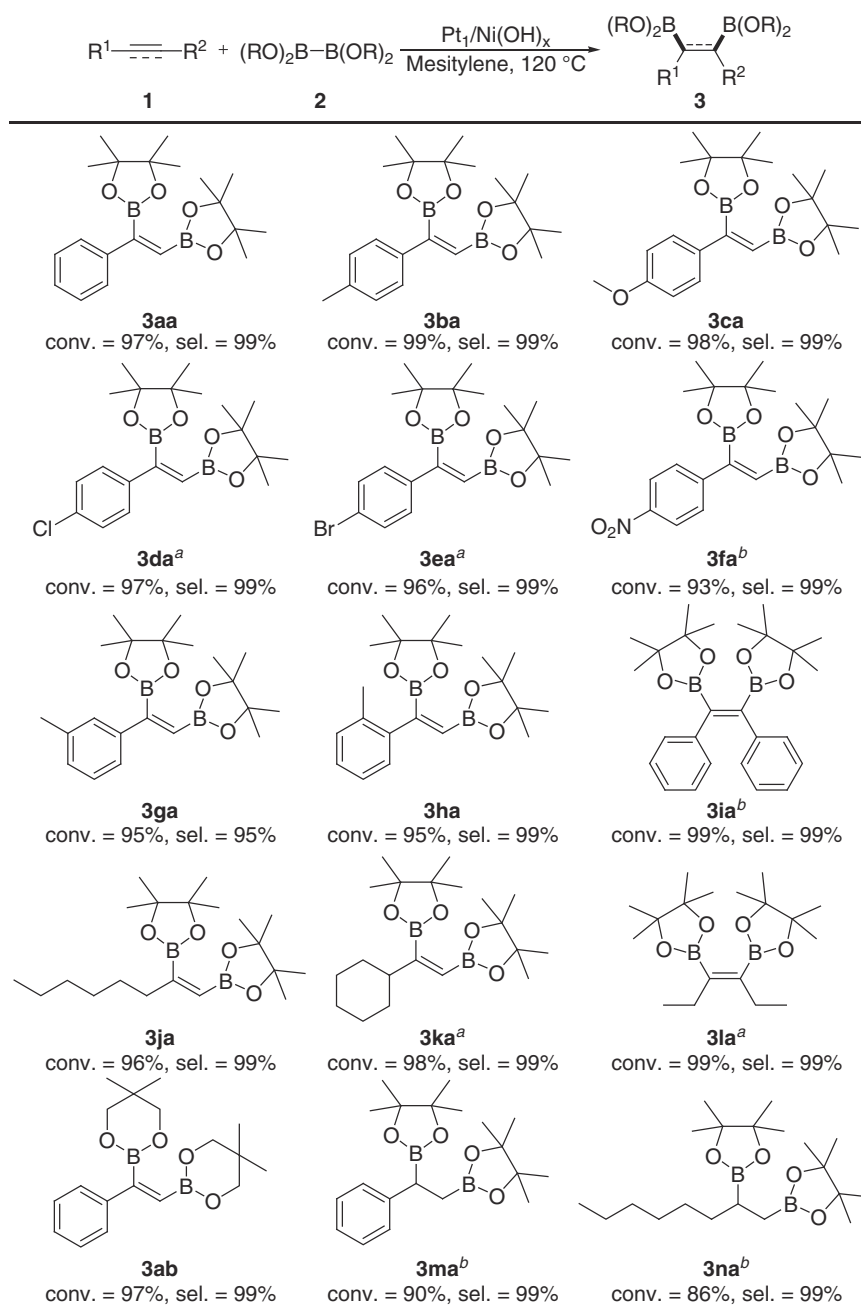
Fig. 3 Substrate scope of diboration reactions over the Pt$_1$/Ni(OH)$_x$ catalyst. Standard reaction conditions: substrate **1** (0.50 mmol) and **2** (0.50 mmol), Pt$_1$/Ni(OH)$_x$ catalyst, Pt/substrate = 0.1%, mesitylene (2.0 mL) as solvent, T = 120 °C, t = 0.3 h. Conversion are determined by gas chromatography (GC) analysis with dodecane as internal standard. Selectivities are determined by GC-MS analysis. [a] t = 1.0 h. [b] t = 6.0 h and substrate **2** (0.75 mmol) was used

under the same conditions as that of Ni(OH)$_x$ NBs (Supplementary Fig. 10). As expected, in the obtained Pt/Ni(OH)$_2$ sample, numbers of Pt nanoparticles are observed clearly on the perfect Ni(OH)$_2$ by HR-TEM (Supplementary Fig. 11), which results in a relatively low catalytic efficiency of Pt/Ni(OH)$_2$ for diboration reactions (Supplementary Table 1, entry 3 and 4). This visible difference indicates that Ni(OH)$_x$ NBs have a stronger interaction with isolated Pt atoms than the perfect Ni(OH)$_2$ to prevent the formation of Pt clusters or nanoparticles.

To explore the nature of this strong interaction, we first carried out the EXAFS spectrometry analysis to probe the atomic structure of these two different nickel hydroxides. As shown in Fig. 4a, the Ni K-edge Fourier-transformed EXAFS spectrum of Ni(OH)$_x$ NBs exhibit an apparent difference in spectral shape compared

with that of the perfect Ni(OH)$_2$, implying the different local atomic arrangement and a defective structure of Ni(OH)$_x$ NBs[51]. Further EXAFS fitting analysis revealed that the values of Debye–Waller factor (σ^2) for the first Ni–O and Ni–Ni shells of Ni(OH)$_x$ NBs are both higher than that of the perfect Ni(OH)$_2$, suggesting a higher degree of disorder in Ni(OH)$_x$ NBs, which is in accord with the polycrystalline structure of Ni(OH)$_x$ NBs (Supplementary Table 2). More importantly, the coordination number (N) of the first Ni–Ni shell of Ni(OH)$_x$ NBs is about 4.8, which is lower than that of the perfect Ni(OH)$_2$ (~6.2), whereas their coordination numbers of the first Ni-O shell are nearly same (~6.0), indicating the formation of Ni^{2+} vacancies in Ni(OH)$_x$ NBs. Many studies show that the formation of Ni^{2+} vacancies will lead some Ni^{2+} ions to transform into Ni^{3+} ions due to the
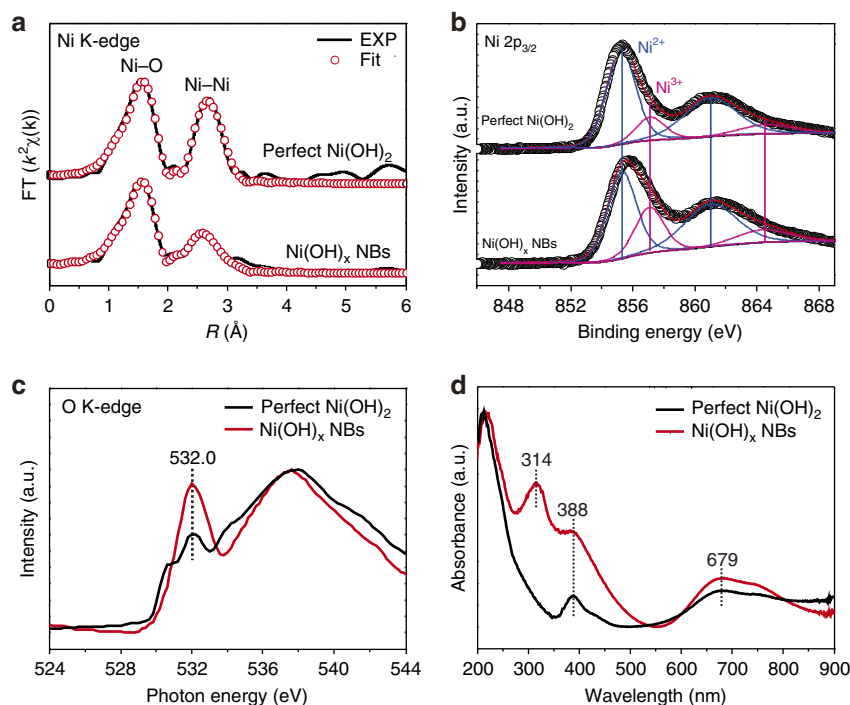
Fig. 4 Investigation of cation vacancies on $Ni(OH)_x$ NBs. **a** Ni K-edge Fourier transform EXAFS spectra and corresponding fitting analysis for $Ni(OH)_x$ NBs and the perfect $Ni(OH)_2$. **b** XPS analysis of $Ni(OH)_x$ NBs and the perfect $Ni(OH)_2$ in the Ni $2p_{3/2}$ region. **c** O K-edge sXAS spectra of $Ni(OH)_x$ NBs and the perfect $Ni(OH)_2$. **d** UV-Vis DRS spectrum of $Ni(OH)_x$ NBs compared with the perfect $Ni(OH)_2$

charge neutrality[52]. Hence, we carried out XPS measurements to detect the Ni^{3+} ions in the $Ni(OH)_x$ NBs. Figure 4b displays the representative XPS spectrum in Ni $2p_{3/2}$ region of $Ni(OH)_x$ NBs and the perfect $Ni(OH)_2$, which can be deconvoluted into four peaks. The signal of Ni^{3+} ions can be clearly distinguished from that of Ni^{2+} ions (centered at 855.3 eV and 861.0 eV) with higher binding energies at 857.2 eV and 864.7 eV, respectively, which correspond with the data reported[53–55]. Distinctly, unlike the perfect $Ni(OH)_2$, $Ni(OH)_x$ NBs display a stronger signal of Ni^{3+} ions, manifesting the possession of more Ni^{3+} ions in the $Ni(OH)_x$ NBs. The proof of Ni^{3+} ions in $Ni(OH)_x$ NBs is garnered from the soft XAS (sXAS) analysis, too. As shown in Fig. 4c, the obviously increased intensity at 532.0 eV (Ni–O interaction) at O K-edge of $Ni(OH)_x$ NBs relative to that of the perfect $Ni(OH)_2$ suggests that electrons transfer intensively from oxygen to nickel, which is consistent with the presence of Ni^{3+} ions[56–58]. In addition, the ultraviolet-visible diffuse reflectance spectroscopy (UV-Vis DRS) experiments also evidence the Ni^{3+} ions in $Ni(OH)_x$ NBs. As can be seen from Fig. 4d, besides the two absorption bands of Ni^{2+} ions at 388 nm and 679 nm in the both two samples, a unique absorption band of $Ni(OH)_x$ NBs appears at 314 nm and is characteristic of Ni^{3+} ions[59,60]. On the basis of all above evidences, we conclude that abundant Ni^{2+} vacancies exist on the $Ni(OH)_x$ NBs and induce the strong interaction with isolated Pt atoms.

To gain more insight into the interaction between Ni^{2+} vacancies and isolated Pt atoms, density functional theory (DFT) calculations were conducted to verify the different formation energies of the isolated Pt atoms loaded on the $Ni(OH)_2$ with and without Ni^{2+} vacancies (for details, see Supplementary Methods section). As can be seen from Fig. 5, the Pt atom adsorbed on the $Ni(OH)_2$ with Ni^{2+} vacancies displays a formation energy at −3.89 eV, which is much lower than that of the Pt atom adsorbed on the $Ni(OH)_2$ without Ni^{2+} vacancies (at −0.72 eV). For the $Ni(OH)_2$ with Ni^{2+} vacancies, the most stable adsorption site for the Pt atom is found to be the Ni^{2+} vacancy site as well as the three-

fold hollow site of the oxygen atoms, and the Pt atom is fixed by the three top oxygen atoms near to the Ni^{2+} vacancy according to the charge density difference (Fig. 5a). In contrast, the Pt atom on the $Ni(OH)_2$ without Ni^{2+} vacancies tends to locate at the site slightly deviated from three-fold hollow site of oxygen atoms, which is caused by the competition between the strong interaction between the Pt atom and three top oxygen atoms and the electrostatic repulsion between positive charged Pt and Ni atoms (Fig. 5b). Furthermore, the oxidation states of isolated Pt atoms anchored on the $Ni(OH)_2$ with and without Ni^{2+} vacancies were also estimated by evaluating Bader charges of the Pt atoms in the film and by normalizing them to Bader charges of PtO_2 (for details, see Supplementary Methods section). As a result, the oxidation state of the Pt atom on the $Ni(OH)_2$ with Ni^{2+} vacancies is +3.55, which is higher than that on the $Ni(OH)_2$ without Ni^{2+} vacancies (+2.70) and very compatible with the aforementioned XANES data of $Pt_1/Ni(OH)_x$ in Fig. 2b. This higher oxidation state illustrates the increase of charge transfer from the support to the Pt atoms[4]. In terms of these DFT calculation results and the XANES data, it is convinced that the Ni^{2+} vacancies play a vital role in the stabilization of isolated Pt atoms deposited on the $Ni(OH)_x$ by eliminating the spatial segregation between the Pt atoms and uncoordinated O atoms, as well as decreasing the formation energy of the Pt atoms through promoting charge transfer from $Ni(OH)_x$ to them. Further DFT calculations on the catalytic mechanism of the $Pt_1/Ni(OH)_x$ catalyst for diboration reactions even disclosed that the Ni^{2+} vacancies not only play an important role in locating isolated Pt atoms but also are conducive to the diboration reactions because the low-coordination oxygen atoms at the vacancy site around the located Pt atoms benefit the dissociation of B–B bonds (for details, see Supplementary Methods section).

In summary, we report that a defect-rich $Ni(OH)_x$ NBs supported SAS Pt catalyst with remarkable performance in diboration reactions. The $Ni(OH)_x$ NBs with a polycrystalline structure are newly synthesized and successfully loaded with SAS Pt to a high
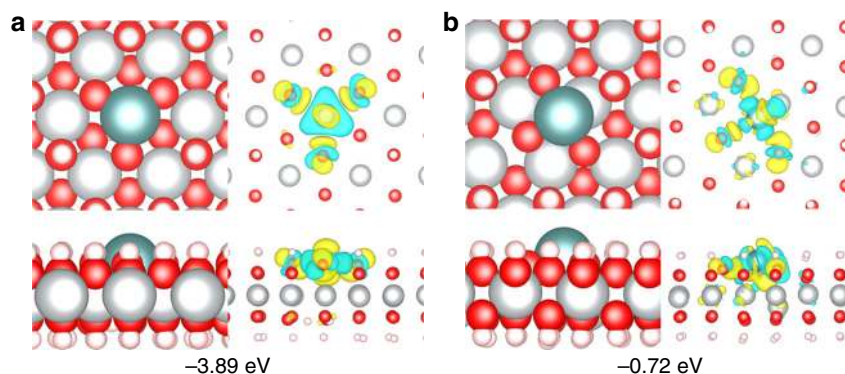
Fig. 5 Studies of the interaction between Ni^{2+} vacancies and isolated Pt atoms. Top and side views of the most stable structure and charge density difference for the Pt atom adsorbed on the $Ni(OH)_2$ with Ni^{2+} vacancies (**a**) and without Ni^{2+} vacancies (**b**). The cyan, gray, red, and white balls refer to Pt, Ni, O, and H atoms, respectively. For charge density difference, yellow (blue) corresponds to charge accumulation (depletion) plotted with an isovalue of $\pm 0.01\,e\,\text{Å}^{-3}$

content as 2.3 wt% just through a simple wet impregnation method. Different from common perfect $Ni(OH)_2$, this defective $Ni(OH)_x$ is abundant in Ni^{2+} vacancy defects that play a key role in stabilizing the Pt atoms at single atomic sites via an enhanced charge-transfer mechanism. The as-fabricated $Pt_1/Ni(OH)_x$ catalyst displays a good activity and selectivity in diboration of various alkynes and alkenes, and the greatest $TOF_{overall}$ value upon reaction completion can reach up to around $3000\,h^{-1}$, which is much higher than other heterogeneous catalysts reported in the literatures. Finally, our work suggests that SAS catalysts might open up new opportunities in heterogenization of homogeneous catalytic reactions for improved activity, and making use of the cation vacancy defects on supports to anchor the guest metal atoms would become a valid approach to prepare these SAS catalysts.

Methods

Synthesis of $Ni(OH)_x$ NBs. $Ni(NO_3)_2 \cdot 6H_2O$ (2.5 mmol, 725.0 mg) was dissolved in deionized water (10 mL) and triethylene glycol (20 mL) and then mixed with an aqueous solution of urea (5.0 mmol, 300.0 mg), TBAH (25% aqueous solution, 0.8 mmol, 0.8 mL), and $NaHCO_3$ (1.5 mmol, 126.0 mg) in deionized water (10 mL). After vigorous stirring for 15 min at ambient temperature, the mixture was transferred into a 50-mL Teflon-lined stainless-steel autoclave and heated at 120 °C for 12 h. The green product was collected via centrifugation and further washed with deionized water and ethanol for two times, respectively. After drying in vacuum oven, the $Ni(OH)_x$ NBs were used for characterization and further preparation.

Synthesis of the $Pt_1/Ni(OH)_x$ catalyst. The as-synthesized $Ni(OH)_x$ NBs (100.0 mg) were first dispersed in 20 mL ethanol under ultrasonic vibration. A H_2PtCl_6 solution (6.3 mg in 5 mL ethanol) was next added dropwise into the $Ni(OH)_x$ NBs dispersion under stirring at ambient temperature. After continuous stirring overnight, the suspension was centrifuged. The recovered solid was then dried in vacuum oven and reduced in 5% H_2/N_2 at 100 °C for 2 h to afford the $Pt_1/Ni(OH)_x$ catalyst for further characterization and catalysis test.

Synthesis of the perfect $Ni(OH)_2$ and $Pt/Ni(OH)_2$. The conventional perfect $Ni(OH)_2$ were prepared by following a modified synthetic method in the literature[61]. In a typical procedure, $Ni(NO_3)_2 \cdot 6H_2O$ (5.0 mmol, 1.45 g) and urea (20.0 mmol, 1.20 g) were dispersed in a mixture containing deionized water (10 mL) and triethylene glycol (70 mL) under vigorous stiring. The final solution was sealed in a 100-mL Teflon-lined stainless-steel autoclave and heated at 100 °C for 6 h. The perfect $Ni(OH)_2$ were obtained by centrifugation and further washed with deionized water and ethanol for two times, respectively. Finally, they were dried at 70 °C for 12 h before characterization and further preparation. With the as-prepared perfect $Ni(OH)_2$ as the support, the $Pt/Ni(OH)_2$ was synthesized through the same procedure of the fabrication of $Pt_1/Ni(OH)_x$ catalyst aforementioned but with a more dilute H_2PtCl_6 solution (2.1 mg in 5 mL ethanol).

Measurements of diboration reactions. All manipulations were carried out using standard Schlenk techniques. Unless otherwise noted, analytical grade solvents and commercially available reagents were used as received. In a typical procedure, alkynes or alkenes (0.5 mmol), B_2pin_2 (0.5 mmol), and $Pt_1/Ni(OH)_x$ (Pt/substrate = 0.1%) were placed in a Shlenck tube equipped with a stir bar, and then mesitylene (2.0 mL) was injected and the mixture was stirred at 120 °C for the corresponding reaction time. After the reaction was completed, the reaction mixture was analyzed by GC and GC-MS with dodecane as the internal standard. The overall TOF value was measured upon completion of reactions and the calculation of it was based on the total Pt loading in the catalyst.

Characterization. TEM images were taken from a Hitachi H-800 transmission electron microscope operated at 100 kV. HR-TEM, STEM, and EDX elemental mapping characterizations were carried out on a JEOL JEM-2100F field emission transmission electron microscope operated at 200 kV. The AC-HAADF STEM characterization was conducted on a Titan 80–300 scanning/transmission electron microscope operated at 300 kV, equipped with a probe spherical aberration corrector. XPS data were collected from a Thermo Fisher Scientific ESCALAB 250Xi XPS System, and the binding energy of the C1s peak at 284.8 eV was taken as an internal reference. The O K-edge sXAS spectra were collected at BL12B station of National Synchrotron Radiation Laboratory (NRSL) in Hefei, China. EXAFS spectra at Pt L_3-edge and Ni K-edge and the XANES spectra at Pt L_3-edge were all collected at the 1W1B station in Beijing Synchrotron Radiation Facility in transmission mode using a fixed-exit Si (111) double crystal monochromator. The incident X-ray beam was monitored by an ionization chamber filled with N_2, and the acquired EXAFS data were processed according to the standard procedures using the ATHENA module implemented in the IFEFFIT software packages. XRD data were acquired from a Rigaku RU-200b X-ray powder diffractometer with Cu Kα radiation ($\lambda = 1.5406$ Å). ICP-OES measurements were conducted on a Thermo Fisher iCAP™ 7000 Series ICP-OES analyzer. FT-IR spectroscopy was performed on a Bruker V70 infrared spectrometer in the frequency of 600–4000 cm^{-1}. UV-Vis DRS spectra were acquired from a Hitachi U-3900 UV–vis spectrophotometer. The GC analysis was conducted on a Thermo Trace 1300 series GC with a FID detector using a capillary column (TR-5MS, from Thermo Scientific, length 30 m, i.d. 0.25 mm, film 0.25 μm). The GC-MS analysis was carried out on a ISQ GC-MS with a ECD detector (Thermo Trace GC Ultra) using a capillary column (TR-5MS, from Thermo Scientific, length 30 m, i.d. 0.25 mm, film 0.25 μm). ^1H nuclear magnetic resonance (NMR) and ^{13}C NMR data were recorded with a Bruker Advance III (400 MHz) spectrometer. High-resolution exact mass measurements were performed on Thermo Scientific Q Exactive mass spectrometer. The detailed characterization data of products in the article are present in the Supplementary Methods section, and for the corresponding NMR spectra, see Supplementary Figs. 14–43.

Data availability. The data supporting this study are available from the authors upon reasonable request.

References

1. Yang, X. F. et al. Single-atom catalysts: a new frontier in heterogeneous catalysis. *Acc. Chem. Res.* **46**, 1740–1748 (2013).
2. Flytzani-Stephanopoulos, M. & Gates, B. C. Atomically dispersed supported metal catalysts. *Annu. Rev. Chem. Biomol. Eng.* **3**, 545–574 (2012).

3. Thomas, J. M. Catalysis: tens of thousands of atoms replaced by one. *Nature* **525**, 325–326 (2015).

4. Qiao, B. et al. Single-atom catalysis of CO oxidation using Pt$_1$/FeO$_x$. *Nat. Chem.* **3**, 634–641 (2011).

5. Liu, P. et al. Photochemical route for synthesizing atomically dispersed palladium catalysts. *Science* **352**, 797–801 (2016).

6. Guo, X. et al. Direct, nonoxidative conversion of methane to ethylene, aromatics, and hydrogen. *Science* **344**, 616–619 (2014).

7. Kyriakou, G. et al. Isolated metal atom geometries as a strategy for selective heterogeneous hydrogenations. *Science* **335**, 1209–1212 (2012).

8. Fan, L. et al. Atomically isolated nickel species anchored on graphitized carbon for efficient hydrogen evolution electrocatalysis. *Nat. Commun.* **7**, 10667 (2016).

9. Fei, H. et al. Atomic cobalt on nitrogen-doped graphene for hydrogen generation. *Nat. Commun.* **6**, 8668 (2015).

10. Lucci, F. R. et al. Selective hydrogenation of 1,3-butadiene on platinum-copper alloys at the single-atom limit. *Nat. Commun.* **6**, 8550 (2015).

11. Mao, K. et al. A theoretical study of single-atom catalysis of CO oxidation using Au embedded 2D *h*-BN monolayer: a CO-promoted O$_2$ activation. *Sci. Rep.* **4**, 5441 (2014).

12. Abbet, S. et al. Acetylene cyclotrimerization on supported size-selected Pd$_n$ clusters (1≤n≤30): one atom is enough! *J. Am. Chem. Soc.* **122**, 3453–3457 (2000).

13. Gong, X. Q., Selloni, A., Dulub, O., Jacobson, P. & Diebold, U. Small Au and Pt clusters at the anatase TiO$_2$(101) surface: behavior at terraces, steps, and surface oxygen vacancies. *J. Am. Chem. Soc.* **130**, 370–381 (2008).

14. Matthey, D. et al. Enhanced bonding of gold nanoparticles on oxidized TiO$_2$(110). *Science* **315**, 1692–1696 (2007).

15. Wu, P., Du, P., Zhang, H. & Cai, C. Graphyne-supported single Fe atom catalysts for CO oxidation. *Phys. Chem. Chem. Phys.* **17**, 1441–1449 (2015).

16. Sun, S. et al. Single-atom catalysis using Pt/graphene achieved through atomic layer deposition. *Sci. Rep.* **3**, 1775 (2013).

17. Jia, Q. et al. Experimental observation of redox-induced Fe-N switching behavior as a determinant role for oxygen reduction activity. *ACS Nano* **9**, 12496–12505 (2015).

18. Wang, H. et al. Doping monolayer graphene with single atom substitutions. *Nano Lett.* **12**, 141–144 (2012).

19. Bliem, R. et al. Subsurface cation vacancy stabilization of the magnetite (001). *Surf. Sci.* **346**, 1215–1218 (2014).

20. Qiao, B. et al. Ultrastable single-atom gold catalysts with strong covalent metal-support interaction (CMSI). *Nano Res.* **8**, 2913–2924 (2015).

21. Qiao, B. et al. Highly efficient catalysis of preferential oxidation of CO in H$_2$-rich stream by gold single-atom catalysts. *ACS Catal.* **5**, 6249–6254 (2015).

22. Peterson, E. J. et al. Low-temperature carbon monoxide oxidation catalysed by regenerable atomically dispersed palladium on alumina. *Nat. Commun.* **5**, 4885 (2014).

23. Hahn, B. P., Long, J. W. & Rolison, D. R. Something from nothing: enhancing electrochemical charge storage with cation vacancies. *Acc. Chem. Res.* **46**, 1181–1191 (2013).

24. Li, F. & Duan, X. *Layered Double Hydroxides* (Springer, Berlin, Heidelberg, 2006).

25. Miyaura, N. & Suzuki, A. Palladium-catalyzed cross-coupling reactions of organoboron compounds. *Chem. Rev.* **95**, 2457–2483 (1995).

26. Jakle, F. Borylated polyolefins and their applications. *J. Inorg. Organomet. Polym. Mater.* **15**, 293–307 (2005).

27. Hawthorne, M. F. & Maderna, A. Applications of radiolabeled boron clusters to the diagnosis and treatment of cancer. *Chem. Rev.* **99**, 3421–3434 (1999).

28. Burgess, K. & Ohlmeyer, M. J. Transition-metal-promoted hydroborations of alkenes, emerging methodology for organic transformations. *Chem. Rev.* **91**, 1179–1191 (1991).

29. Takaya, J. & Iwasawa, N. Catalytic, direct synthesis of bis(boronate) compounds. *ACS Catal.* **2**, 1993–2006 (2012).

30. Ishiyama, T., Matsuda, N., Miyaura, N. & Suzuki, A. Platinum(0)-catalyzed diboration of alkynes. *J. Am. Chem. Soc.* **115**, 11018–11019 (1993).

31. Ishiyama, T. et al. Platinum(0)-catalyzed diboration of alkynes with tetrakis (alkoxo)diborons: an efficient and convenient approach to cis-bis(boryl) alkenes. *Organometallics* **15**, 713–720 (1996).

32. Ansell, M. B. et al. An experimental and theoretical study into the facile, homogeneous (N-heterocyclic carbene)2-Pd-0(0) catalyzed diboration of internal and terminal alkynes. *Catal. Sci. Technol.* **6**, 7461–7467 (2016).

33. Morgan, J. B. & Morken, J. P. Catalytic enantioselective hydrogenation of vinyl bis(boronates). *J. Am. Chem. Soc.* **126**, 15338–15339 (2004).

34. Ansell, M. B., Navarro, O. & Spencer, J. Transition metal catalyzed element–element′ additions to alkynes. *Coord. Chem. Rev.* **336**, 54–77 (2017).

35. Neeve, E. C., Geier, S. J., Mkhalid, I. A., Westcott, S. A. & Marder, T. B. Diboron(4) compounds: from structural curiosity to synthetic workhorse. *Chem. Rev.* **116**, 9091–9161 (2016).

36. Braunschweig, H. et al. Synthesis, reactivity, and electronic structure of [*n*] vanadoarenophanes: an experimental and theoretical study. *J. Am. Chem. Soc.* **130**, 11376–11393 (2008).

37. Chen, Q. et al. Remarkable catalytic property of nanoporous gold on activation of diborons for direct diboration of alkynes. *Org. Lett.* **15**, 5766–5769 (2013).

38. Alonso, F., Moglie, Y., Pastor-Perez, L. & Sepulveda-Escribano, A. Solvent-and ligand-free diboration of alkynes and alkenes catalyzed by platinum nanoparticles on titania. *Chemcatchem* **6**, 857–865 (2014).

39. Grirrane, A., Corma, A. & Garcia, H. Stereoselective single (copper) or double (platinum) boronation of alkynes catalyzed by magnesia-supported copper oxide or platinum nanoparticles. *Chem.* **17**, 2467–2478 (2011).

40. Wang, L. et al. Optimizing the Volmer step by single-layer nickel hydroxide nanosheets in hydrogen evolution reaction of platinum. *ACS Catal.* **5**, 3801–3806 (2015).

41. Yin, H. et al. Ultrathin platinum nanowires grown on single-layered nickel hydroxide with high hydrogen evolution activity. *Nat. Commun.* **6**, 6430 (2015).

42. Xu, H., Ding, L. X., Feng, J. X. & Li, G. R. Pt/Ni(OH)$_2$-NiOOH/Pd multi-walled hollow nanorod arrays as superior electrocatalysts for formic acid electrooxidation. *Chem. Sci.* **6**, 6991–6998 (2015).

43. Wang, D., Yan, W., Vijapur, S. H. & Botte, G. G. Enhanced electrocatalytic oxidation of urea based on nickel hydroxide nanoribbons. *J. Power Sources* **217**, 498–502 (2012).

44. Yang, D., Wang, R., Zhang, J. & Liu, Z. Synthesis of nickel hydroxide nanoribbons with a new phase: a solution chemistry approach. *J. Phys. Chem. B.* **108**, 7531–7533 (2004).

45. Li, W., Comotti, M. & Schuth, F. Highly reproducible syntheses of active Au/ TiO$_2$ catalysts for CO oxidation by deposition–precipitation or impregnation. *J. Catal.* **237**, 190–196 (2006).

46. Zhou, Z. et al. Preparation of highly active Pt/C cathode electrocatalysts for DMFCs by an improved aqueous impregnation method. *Phys. Chem. Chem. Phys.* **5**, 5485–5488 (2003).

47. Mori, K., Taga, T. & Yamashita, H. Isolated single-atomic Ru catalyst bound on a layered double hydroxide for hydrogenation of CO$_2$ to formic acid. *ACS Catal.* **7**, 3147–3151 (2017).

48. Moses-DeBusk, M. et al. CO oxidation on supported single Pt atoms: experimental and ab initio density functional studies of CO interaction with Pt atom on θ-Al$_2$O$_3$(010) surface. *J. Am. Chem. Soc.* **135**, 12634–12645 (2013).

49. Vile, G. et al. A stable single-site palladium catalyst for hydrogenations. *Angew. Chem. Int. Ed.* **54**, 11265–11269 (2015).

50. Zhang, X., Shi, H. & Xu, B. Q. Catalysis by gold: isolated surface Au^{3+} ions are active sites for selective hydrogenation of 1,3-butadiene over Au/ZrO$_2$ catalysts. *Angew. Chem. Int. Ed.* **44**, 7132–7135 (2005).

51. Huang, W. et al. Highly active and durable methanol oxidation electrocatalyst based on the synergy of platinum-nickel hydroxide-graphene. *Nat. Commun.* **6**, 10035 (2015).

52. Makhlouf, S. A., Kassem, M. A. & Abdel-Rahim, M. A. Particle size-dependent electrical properties of nanocrystalline NiO. *J. Mater. Sci.* **44**, 3438–3444 (2009).

53. Kim, K. S. & Winograd, N. X-ray photoelectron spectroscopic studies of nickel-oxygen surfaces using oxygen and argon ion-bombardment. *Surf. Sci.* **43**, 625–643 (1974).

54. Venezia, A. M., Bertoncello, R. & Deganello, G. X-ray photoelectron-spectroscopy investigation of pumice-supported nickel-catalysts. *Surf. Interface Anal.* **23**, 239–247 (1995).

55. Biesinger, M. C. et al. Resolving surface chemical states in XPS analysis of first row transition metals, oxides and hydroxides: Cr, Mn, Fe, Co and Ni. *Appl. Surf. Sci.* **257**, 2717–2730 (2011).

56. Soriano, L. et al Splitting of Ni 3d states at the surface of NiO nanostructures . *Phys. Rev. B* **74**, 193402 (2006).

57. Pellegrin, E. et al. O 1s near-edge X-ray absorption of La$_{2−x}$Sr$_x$NiO$_{4+δ}$: holes, polarons, and excitons. *Phys. Rev. B* **53**, 10667–10679 (1996).

58. Finazzi, M. & Brookes, N. B. Resonant Auger spectroscopy at the O K edge of NiO. *Phys. Rev. B* **60**, 5354–5358 (1999).

59. Espinos, J. P., Gonzalezelipe, A. R., Caballero, A., Garcia, J. & Munuera, G. The state of nickel in Ni/SiO$_2$ and Ni/TiO$_2$-calcined catalysts. *J. Catal.* **136**, 415–422 (1992).

60. Kimura, E., Sakonaka, A., Machida, R. & Kodama, M. Novel nickel(II) complexes with doubly deprotonated dioxopentaamine macrocyclic ligands for uptake and activation of molecular-oxygen. *J. Am. Chem. Soc.* **104**, 4255–4257 (1982).

61. Du, H., Jiao, L., Cao, K., Wang, Y. & Yuan, H. Polyol-mediated synthesis of mesoporous alpha-Ni(OH)$_2$ with enhanced supercapacitance. *ACS Appl. Mater. Interfaces* **5**, 6643–6648 (2013).

Author contributions

J.Z. performed the experiments, collected and analyzed the data, and wrote the paper. X.W. and J.L. conducted the density functional theory calculation and analysis. W.-C.C. and R.L. assisted in HR-TEM, STEM, and EDX elemental mapping characterizations. W. C. and L.Z. helped with XANES and EXAFS spectrometry analyses. W.Y. helped with the sXAS analysis. L.G. assisted in the AC HAADF-STEM characterization. C.C. and Q.P. helped with data analyses and discussions. D.W. and Y.L. conceived the experiments, planned synthesis, analyzed results, and wrote the paper.

Additional information

Supplementary Information accompanies this paper at https://doi.org/10.1038/s41467-018-03380-z.

Competing interests: The authors declare no competing interests.

Reprints and permission information is available online at http://npg.nature.com/reprintsandpermissions/

Publisher's note: Springer Nature remains neutral with regard to jurisdictional claims in published maps and institutional affiliations.